# Purely thermal-wave photopyroelectric interferometry

Chinhua Wang and Andreas Mandelis[a)]
*Photothermal and Optoelectronic Diagnostics Laboratories (PODL), Department of Mechanical and Industrial Engineering, University of Toronto, 5 King's College Road, Toronto, Ontario, M5S 3G8 Canada*

(Received 22 October 1998; accepted for publication 16 February 1999)

A thermal-wave interferometric technique based on pure thermal-wave interference using two-cavity photopyroelectric (PPE) detection has been developed. The salient features of this interferometry are investigated with a general theory, which describes the dependence of the PPE signal on the optical, thermal, and geometric parameters of the thermal-wave cavity configuration. Preliminary experimental results are presented. A major feature of the technique is the efficient suppression of the background PPE signal base line. The physical origins of the interferometry are also discussed. © *1999 American Institute of Physics.* [S0021-8979(99)02811-X]

## I. INTRODUCTION

The single-beam photopyroelectric (PPE) technique is a well-established photothermal method used for spectroscopic and thermal characterization of various materials as well as for studies of thermophysical properties of gases.[1–9] The basic principle of the single-beam PPE technique is that when a periodically modulated energy source impinges on the surface of a sample, the sample will absorb some of the incident energy and will, in turn, produce a localized temperature increase following a nonradiative deexcitation process. This periodic temperature variation in the sample can be detected with a pyroelectric transducer made of a thin-film pyroelectric material [e.g., polyvinylidene fluoride (PVDF)]. The PPE signal from the pyroelectric transducer is due to a temperature-dependent change in polarization of the pyroelectric material.[1,2] If the sample does not contact the transducer, the air gap formed in the medial region amounts to a thermal-wave cavity. This cavity confines the thermal-wave oscillation and has been shown to give rise to a standing-wave-equivalent structure, the length of which can be tuned to resonant antinode and node patterns.[5] Recently, such thermal-wave resonant cavities have been used for high precision measurements of thermophysical properties of the intracavity gases.[5,8,9,10]

In all the conventional embodiments of the PPE technique,[1,4,7,11] a single excitation source is employed with the radiation impinging on either the front- (PPE), or the rear-surface [inverse PPE (IPPE)] of a PVDF transducer. The sensitivity and dynamic range, however, of the PPE measurement scheme can be compromised in the study of solid transparent materials, due to the substantial base line signal from direct transmission of the incident light onto the detector. In addition, in the case of IPPE, the restriction imposed by the requirement for thermally thin PVDF film and for sample-detector contact further compromises the dynamic range of photopyroelectric sensor devices. Some earlier efforts were made to lower the instrumental base line of PPE detection systems: differential front-surface polarization modulation[12] and out-of-phase sample-surface modulation[6] PPE schemes involve the formation of destructive thermal-wave interference inside the body of a solid sample. They have been used with considerable enhancement of the signal-to-noise ratio owing to base line suppression. Nevertheless, the specific thin-surface-film preparation, vacuum environment, and optical excitation wavelength requirements imposed on the former technique cannot be met by a large number of geometries and materials, which do not exhibit discrete polarization states. Furthermore, bulk thermal inhomogeneities and the strong thermal-wave dispersion inside a solid, photothermally excited by out-of-phase surface modulation of two laser beams clearly limit the dynamic range of the latter technique, which usually results in an incomplete base line suppression, exacerbated with increasing sample thickness.

In this work, the theory and preliminary experimental methodology of a thermal-wave interferometric technique is developed. The technique is based on the spatial interference of thermal waves *within the body of the pyroelectric transducer*, independently of the sample. It has been developed in order to overcome the shortcomings of the earlier interferometric methodologies and may be regarded as the evolution of the method presented in Ref. 6, in that it creates out-of-phase destructive interference patterns between highly aligned thermal waves in the transducer itself, resulting in complete base line suppression. Unlike other prior (''conventional'') photothermal interferometric schemes,[12–15] the new technique is *not* based on monitoring thermal waves resulting from direct optical interference patterns, such as those generated by two appropriately modulated laser beams (e.g., intensity, phase or polarization modulation). In the present coherence scheme, thermal waves are induced by two intensity-modulated beams, split off a single laser source and with a fixed phase shift relationship between them. The usually large instrumental PPE base line signal and a significant portion of the noise can be efficiently suppressed within the PVDF detector if the two laser beams are collinearly incident on opposite surfaces of the thin pyroelectric film,

a)Electronic mail: mandelis@mie.utoronto.ca

 

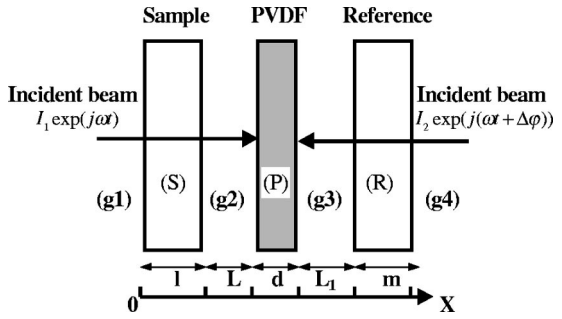


FIG. 1. General PPE geometry for purely thermal-wave interferometry.

and with 180° relative phase shift. In this fashion, much higher signal sensitivity and dynamic range PPE measurements than with the conventional single-beam PPE configurations are expected and have been confirmed very recently in this laboratory. In order to demonstrate the physical principle of this technique, in view of our preliminary experimental results, a general theory is presented, which describes the dependence of the PPE signal from a thin-film PVDF detector on the optical, thermal, and geometric parameters of the dual thermal-wave-cavity configuration, formed by the noncontacting sample, the PVDF and the reference solid. Several special cases of the theory corresponding to various possible experimental configurations are also presented and its advantages over the single-beam noninterferometric PPE method are discussed.

## II. ONE-DIMENSIONAL GENERAL MODEL OF PURELY THERMAL-WAVE PPE INTERFEROMETRY

The most general configuration diagram for purely thermal-wave PPE interferometry using a one-dimensional heat transfer model is shown in Fig. 1. Two laser beams of intensities $I_1$ and $I_2$, respectively, are split off of a laser source and are modulated at the same angular frequency ($\omega$). They have a fixed, adjustable phase shift ($\Delta\varphi$), and are incident onto the front and rear surfaces of a PVDF detector, passing through noncontacting optically transparent sample and reference media, which, along with the PVDF sensor in the middle, form the thermal-wave cavities $g2$ and $g3$ as shown in Fig. 1. The incident beams are assumed to illuminate the PVDF sensor uniformly with spot sizes much larger than the thermal diffusion length in PVDF, so that the one-dimensionality of the heat transfer model is assured. The thickness of the sample, the reference, the PVDF detector and the lengths of cavities $g2, g3$ are $l$, $m$, $d$, $L$ and $L_1$, respectively. The sample and the reference have optical absorption coefficient $\beta_s$, $\beta_r$, respectively. Light absorption by the sample—PVDF transducer—reference system and nonradiative energy conversion to heat increases the temperature of the PVDF sensor, which results in a potential difference between the two surfaces of the transducer due to the photopyroelectric effect. The photopyroelectric signal from the PVDF detector is proportional to the average ac temperature of the PVDF film detector.[7] It is governed by coupled one-dimensional heat diffusion equations subject to appropriate boundary conditions of thermal-wave field and flux continuity across each interface ($g1$-$S$, $S$-$g2$, $g2$-$P$, $P$-$g3$, $g3$-$R$, and $R$-$g4$) of Fig. 1. In the theoretical treatment of the most general case, gaseous media of different thermophysical properties are assumed to exist in regions $g1$, $g2$, $g3$, and $g4$. Assuming negligible radiative heat transfer to the sensor from the heated sample and reference, especially in the case of transparent materials,[9] the appropriate thermal-wave equations have the form

$$\frac{d^2T_i(x)}{dx^2}-\sigma_i^2T_i(x)=0,$$

$$i=1,2,3,4 \text{ for regions } g1,\ g2,\ g3 \text{ and } g4, \tag{1a}$$

$$\frac{d^2T_s(x)}{dx^2}-\sigma_s^2T_s=-\eta_s\beta_s\frac{I_{ts}(x)}{2k_s},\quad 0\leqslant x\leqslant l, \tag{1b}$$

$$\frac{d^2T_p(x)}{dx^2}-\sigma_p^2T_p=0,\quad l+L\leqslant x\leqslant l+L+d, \tag{1c}$$

$$\frac{d^2T_r(x)}{dx^2}-\sigma_r^2T_r=-\eta_r\beta_r\frac{I_{tr}(x)}{2k_r},$$

$$l+L+d+L_1\leqslant x\leqslant l+L+d+L_1+m. \tag{1d}$$

In Eqs. (1), $\sigma_i=(1+j)\sqrt{\omega/2\alpha_i}$ is the complex thermal diffusion coefficient in region $i$ ($i=g1,g2,g3,g4,S,P,R$) with thermal diffusivity $\alpha_i$; $k_s,k_r$ is the thermal conductivity of the sample and the reference, respectively; $\beta_s,\beta_r$ and $\eta_s,\eta_r$ are the optical absorption coefficients and the optical-to-thermal energy conversion coefficients of the sample and the reference, respectively. $I_{ts}(x)$, $I_{tr}(x)$ are the total optical fluence contributions to the depth $x$ in the sample and in the reference media,[3] which are given as follows:

$$I_{ts}(x)=I_1\left[\frac{1-R_s}{1-R_s^2e^{-2\beta_s l}}\right]F_s(x), \tag{2a}$$

$$I_{tr}(x)=I_2e^{j\Delta\varphi}\left[\frac{1-R_r}{1-R_r^2e^{-2\beta_r m}}\right]F_r(x), \tag{2b}$$

where

$$F_s(x)=N_1e^{-\beta_s x}+N_2e^{-\beta_s(2l-x)}, \tag{2c}$$

$$N_1\equiv 1+R_sR_p(1+R_s)e^{-2\beta_s l}, \tag{2d}$$

$$N_2\equiv R_s[1+R_p(1+R_s)] \tag{2e}$$

and

$$F_r(x)=N_{1r}e^{-\beta_r(l+L+d+L_1+m-x)}+N_{2r}e^{-\beta_r[2m-(l+L+d+L_1+m-x)]}, \tag{2f}$$

$$N_{1r}\equiv 1+R_rR_p(1+R_r)e^{-2\beta_r m}, \tag{2g}$$

$$N_{2r}\equiv R_r[1+R_p(1+R_r)]. \tag{2h}$$

In Eqs. (2), $R_s$, $R_r$, $R_p$ are the surface reflectances of the sample, the reference, and the PVDF detector, respectively.

The standard boundary conditions of temperature and heat flux continuity[7] can be used to solve the foregoing

coupled boundary-value problems. In particular, the heat flux boundary conditions at the front and rear surfaces of the PVDF sensor can be written as

$$k_g \frac{dT_2(x)}{dx} - k_p \frac{dT_p(x)}{dx} = (1-R_p) I_1 \frac{(1-R_s)^2}{1-R_s^2 e^{-2\beta_s l}} e^{-\beta_s l}, \quad x = l + L, \tag{3a}$$

$$k_p \frac{dT_p(x)}{dx} - k_g \frac{dT_3(x)}{dx} = (1-R_p) I_2 e^{j\Delta\varphi} \times \frac{(1-R_r)^2}{1-R_r^2 e^{-2\beta_r m}} e^{-\beta_r m}, \quad x = l + L + d, \tag{3b}$$

where the right-hand sides of Eqs. (3a) and (3b) represent the incident beam intensities at the front and rear surfaces of the PVDF thin film, respectively, with due consideration of the infinite set of reflections of the incident beam within the sample and the reference media.[3] The PPE signal from the PVDF detector, assuming a short thermal time constant compared to the inverse of the modulation frequency, can be written as[7]

$$V(\omega) = S(\omega) \int_{l+L}^{l+L+d} T_p(x,\omega)\, dx. \tag{4}$$

Here $S(\omega)$ is the instrumental transfer function, a frequency-dependent factor related to the associated PVDF-signal amplification and processing electronics.[16] It is usually normalized out by means of frequency scans of samples with well-known frequency responses. $T_p(x,\omega)$ is the local complex thermal-wave field in the PVDF, which must be calculated from the above coupled boundary-value problems.

After a considerable amount of algebraic manipulation, the output photopyroelectric signal (voltage mode) for the geometry of Fig. 1 can be finally expressed as follows:

$$V(\omega) = \frac{S(\omega)}{\sigma_p (1+b_{2p})(1+b_{3p})} \times \frac{H_1(1+b_{3p})[G_1(1+W_{21}e^{-2\sigma_2 L}) + 2b_{2p}G_3 e^{-\sigma_2 L}] + H_2(1+b_{2p})[G_2(1+V_{34}e^{-2\sigma_3 L_1}) + 2b_{3p}G_4 e^{-\sigma_3 L_1}]}{[e^{\sigma_p d}(1+\gamma_{3p}V_{34}e^{-2\sigma_3 L_1})(1+\gamma_{2p}W_{21}e^{-2\sigma_2 L}) - e^{-\sigma_p d}(\gamma_{2p}+W_{21}e^{-2\sigma_2 L})(\gamma_{3p}+V_{34}e^{-2\sigma_3 L_1})]}, \tag{5}$$

where

$$b_{ij} = k_i\sqrt{\alpha_j}/k_j\sqrt{\alpha_i}, \tag{6a}$$

$$\gamma_{ij} = (1-b_{ij})/(1+b_{ij}), \tag{6b}$$

$$W_{21} = -\frac{\gamma_{2s}e^{\sigma_s l} - \gamma_{1s}e^{-\sigma_s l}}{e^{\sigma_s l} - \gamma_{2s}\gamma_{1s}e^{-\sigma_s l}}, \tag{6c}$$

$$V_{34} = -\frac{\gamma_{3r}e^{\sigma_r m} - \gamma_{4r}e^{-\sigma_r m}}{e^{\sigma_r m} - \gamma_{3r}\gamma_{4r}e^{-\sigma_r m}}, \tag{6d}$$

$$G_1 = \frac{(1-R_p)}{k_p\sigma_p} \times \frac{I_1(1-R_s)^2}{1-R_s^2 e^{-2\beta_s l}} e^{-\beta_s l}, \tag{6e}$$

$$G_2 = \frac{(1-R_p)}{k_p\sigma_p} \times \frac{I_2 e^{j\Delta\varphi}(1-R_r)^2}{1-R_r^2 e^{-2\beta_r m}} e^{-\beta_r m}. \tag{6f}$$

Expressions for $H_1$, $H_2$ and $G_3$, $G_4$ are given in the Appendix. From the structure of the PPE output voltage of Eq. (5), it can be seen that the first term in the numerator represents the contribution from the front beam, through the sample and the intracavity gas layer $g2$. The second term originates from the rear incident beam, through the reference layer and the intracavity gas layer $g3$. Therefore, the overall output signal is the result of the complex (vectorial) superposition of two thermal wave fields within the PVDF detector generated by two incident laser beams of equal fluences modulated with a fixed phase shift $\Delta\varphi$.

## III. SPECIAL CASES

Equation (5) explicitly demonstrates that the general PPE output signal from the system shown in Fig. 1 is a function of the solid sample and the reference, as well as the constituents of the two thermal-wave cavities formed between the PVDF film and the two solids on either side. The complicated dependence of the signal on the parameters of this system, however, makes any specific physical insight into Eq. (5) very difficult in the general case. Therefore, in this work it is instructive to consider several special cases of theoretical and practical importance, according to several possible configurations among the incident beams, the sample and the reference.

### A. Single laser beam; no reference medium; one (front) thermal-wave cavity

If the rear laser beam and the reference medium are absent, or if the rear beam is absent and the reference solid is placed far away from the PVDF compared to the thermal diffusion length in the gaseous cavity $g3$, then in terms of the foregoing model we must set $I_2 = 0$ and either $m = 0$ (in the absence of a reference solid), or $e^{-\sigma_3 L_1} \to 0$ (if the reference is placed far away from the detector). In both cases Eq. (5) reduces to the following simplified expression:

$$V(\omega)=\frac{S(\omega)}{\sigma_p(1+b_{2p})}\cdot\frac{(e^{\sigma_p d}-1+\gamma_{3p}-\gamma_{3p}e^{-\sigma_p d})[G_1(1+W_{21}e^{-2\sigma_2 L})+2b_{2p}G_3e^{-\sigma_2 L})]}{e^{\sigma_p d}(1+\gamma_{2p}W_{21}e^{-2\sigma_2 L})-\gamma_{3p}e^{-\sigma_p d}(\gamma_{2p}+W_{21}e^{-2\sigma_2 L})}. \tag{7}$$

Equation (7) gives the general expression corresponding to the single-beam PPE technique.[3] In the present case, however, the finite thickness of the PVDF sensor is account for. In the earlier theoretical treatment[3] the PVDF was assumed to be semi-infinite. Figure 2 shows the effect of the finite thickness of the PVDF element on the output signal for a fixed cavity length, $L=200\ \mu$m (see Fig. 1). It was assumed that the transparent sample is a Ti-sapphire laser crystal disk with a thickness of 0.1295 cm[3] and the gaseous media on both sides of the PVDF detector are the same (air). The parameters which were used in Eq. (7) for the simulation are: $k_p=1.3\times10^{-3}$ W/cm K, $\alpha_p=5.4\times10^{-4}$ cm$^2$/s;[15] $k_s=0.33$ W/cm K, $\alpha_s=0.106$ cm$^2$/s;[3] $k_2=k_3=k_{\rm air}=2.62\times10^{-4}$ W/cm K, $\alpha_2=\alpha_3=\alpha_{\rm air}=0.22$ cm$^2$/s;[5] modulation frequency $f=10$ Hz. It can be seen from Fig. 2 that the PPE output signal depends on the thickness of the PVDF detector in the thermally thin range.[7] With increased thickness, the thermally thick condition prevails:[7] the amplitude of the output signal exhibits the expected oscillatory behavior with a global maximum at thickness $\sim40\ \mu$m, before reaching a constant (thermally thick) value; and the phase decreases monotonically before assuming a constant (thermally thick) value. Figure 2 shows that for the foregoing parameters, the PVDF film may be assumed ''semi-infinite'' if its thickness is greater than $\sim200\ \mu$m. Figure 3 shows the output signal (amplitude and phase) as a function of the front cavity length, $L$, formed between a Ti-sapphire sample and the PVDF detector, with the sensor thickness as a parameter. The output PPE signal amplitude peak position shows some shift to longer cavity lengths with increasing PVDF thickness, while the overall phase lag decreases. This is physically as expected, because thinner transducers confine the composite thermal-wave centroid closer to the far wall of the cavity (origin), as witnessed by the amplitude shift toward the origin, and the decreased phase lag. Therefore, for quantitative analysis it is of practical importance to take into account the thickness of the pyroelectric transducer for PVDF films thinner than $\sim200\ \mu$m, as is usually the case with PPE measurements.[1–10] If the thickness of the PVDF is assumed to be semi-infinite, Eq. (7) reduces, as expected, to the single-beam expression given as Eq. (11) in Ref. 3.

### B. Two laser beams; no sample or reference; no thermal-wave cavity

If both sample and reference are absent [or both sample and reference are placed in the optical transmission (OT) mode $(L,L_1\to\infty)$], the following limiting values must be set in Fig. 1: $l=0$, $m=0$, (or $e^{-\sigma_2 L}\to0$, $e^{-\sigma_3 L_1}\to0$), and $R_s=0$, $R_r=0$. In both cases, Eq. (5) is simplified to

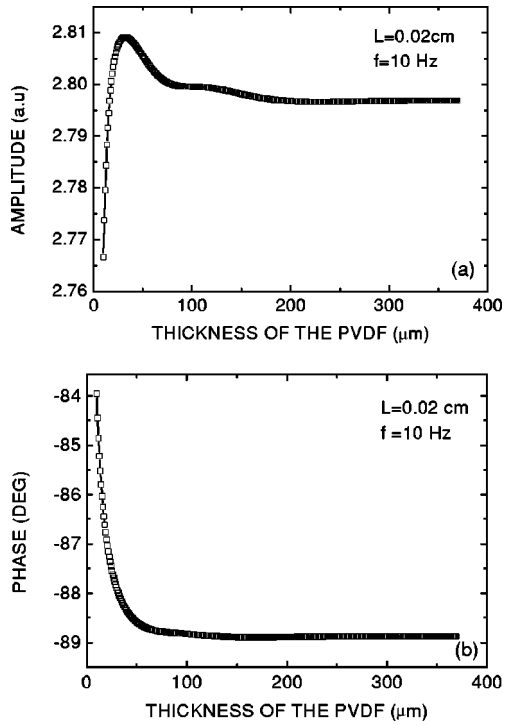


FIG. 2. Effect of the PVDF detector thickness on the output PPE signal; (a) amplitude; (b) phase.

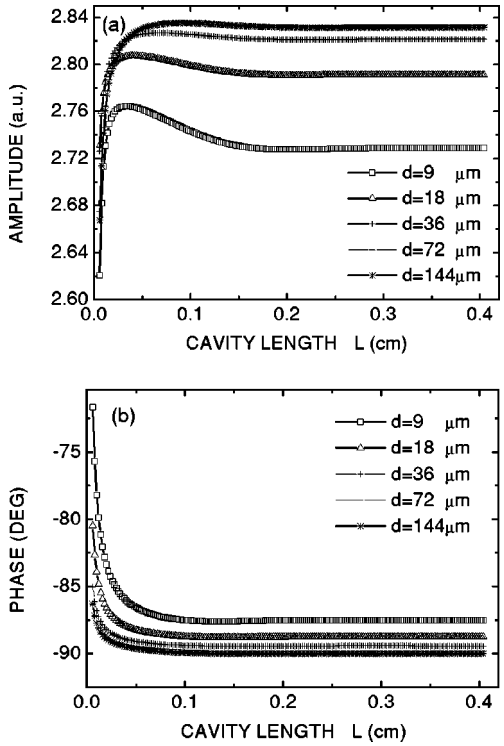


FIG. 3. The output PPE signal vs cavity length $L$, using PVDF detectors of different thickness; (a) amplitude, (b) phase. The parameters used are the same as those of Fig. 2.

$$V(\omega)=\frac{S(\omega)(1-R_p)}{k_p\sigma_p^2}\cdot\frac{I_1(1+b_{3p})\xi_1+I_2e^{j\Delta\varphi}(1+b_{2p})\xi_2}{(1+b_{2p})(1+b_{3p})(e^{\sigma_p d}-\gamma_{2p}\gamma_{3p}e^{-\sigma_p d})}, \quad (8a)$$

where

$$\xi_1\equiv e^{\sigma_p d}-1+\gamma_{3p}-\gamma_{3p}e^{-\sigma_p d},$$

and

$$\xi_2\equiv e^{\sigma_p d}-1+\gamma_{2p}-\gamma_{2p}e^{-\sigma_p d}.$$

If the experimental system is exposed to the same ambient gas medium (usually, air) on both sides of the transducer, then subscripts $2=3=g$ in Eq. (8a), which further reduces to

$$V(\omega)=\frac{S(\omega)(1-R_p)}{k_p\sigma_p^2(1+b_{\mathrm{gp}})}\cdot\frac{[I_1+I_2e^{j\Delta\varphi}](e^{\sigma_p d}-1+\gamma_{\mathrm{gp}}-\gamma_{\mathrm{gp}}e^{-\sigma_p d})}{e^{\sigma_p d}-\gamma_{\mathrm{gp}}^2e^{-\sigma_p d}}. \quad (8b)$$

This is the simplest case of coherent interference of two thermal waves of different amplitudes, which are generated directly within the PVDF detector by two oppositely incident laser beams of arbitrary fluence and arbitrary phase shift. Equation (8b) shows that constructive or destructive interference patterns will appear when the relative phase shift $\Delta\varphi=0°$ or 180°, respectively. Figure 4 shows the amplitude and phase of the interference-generated PPE signal, Eq. (8b), as functions of the phase shift $\Delta\varphi$ at different fluence ratios of the two laser beams. The parameters used in the simulation are: $I_1=1.0\,\mathrm{W/m^2}$, $d=52\,\mu$m. Other parameters are the same as those used in Fig. 2. It is observed in Fig. 4 that the fully destructive interference pattern occurs in the amplitude channel when $I_2/I_1=1$ and only for odd integral multiples of 180°, curve b, while the phase increases linearly with increasing phase shift. A large constant base line PPE signal appears in the case of $I_2/I_1=0$ (i.e., the single-beam case), curve a, independent of $\Delta\varphi$, characteristic of complete absence of thermal-wave interference, as expected. Comparing the two foregoing patterns, the advantage of the situation depicted by curve b at the nodes becomes immediately apparent in terms of the large coherent base line signal suppression, theoretically to zero level. In this mode, the thermal-wave interferometer acts as a sensitive detector of purely optical radiation variations between the intensities of the two incident beams. In practice, one is left with the residual experimental system noise under full destructive interference: experimentally, we found that if we use a 5 mW laser beam modulated at 10 Hz, we obtain an output PPE signal $V_0\sim3$ mV by blocking the rear incident beam. Under the same experimental conditions, we can easily obtain a minimum interference output signal $V_i\sim1\,\mu$V for fully destructive interference. This represents a figure-of-merit (FOM$=V_0/V_i$) of the PPE thermal-wave interferometer of $\sim3000$. Under these conditions, a very small variation in output signal on the order of 1 $\mu$V caused by an intensity change of the front laser beam as a result of an optical or photothermal fluctuation can be readily sensed by a fully destructive thermal-wave interferometer with practical resolution of 0.1 $\mu$V.[17] By contrast, the same variation in the output signal is impossible to detect with the single-beam method with practical resolution of 0.01 mV. It should be noted that conventional optical detectors such as photodiodes, cannot exhibit such high FOM, because the protective transparent overlayer and/or the nonnormal incidence of two laser beams on the active area (front surface) of the detector make it harder to produce precise spatial symmetries, coincidence and equal spot sizes. Therefore, optical detectors are capable of only partial fluence (and thus base line) cancellation, as equivalently shown by the intermediate case of partially destructive interference in Fig. 4(a), curve c. This is not a problem using the simple normal incidence arrangement from both sides of the PPE interferometer depicted in Fig. 1. Thus, unlike conventional optical detectors, the PPE fully destructive interferometer has the potential to be an optimum FOM instrument for optical beam power/fluence characterization.

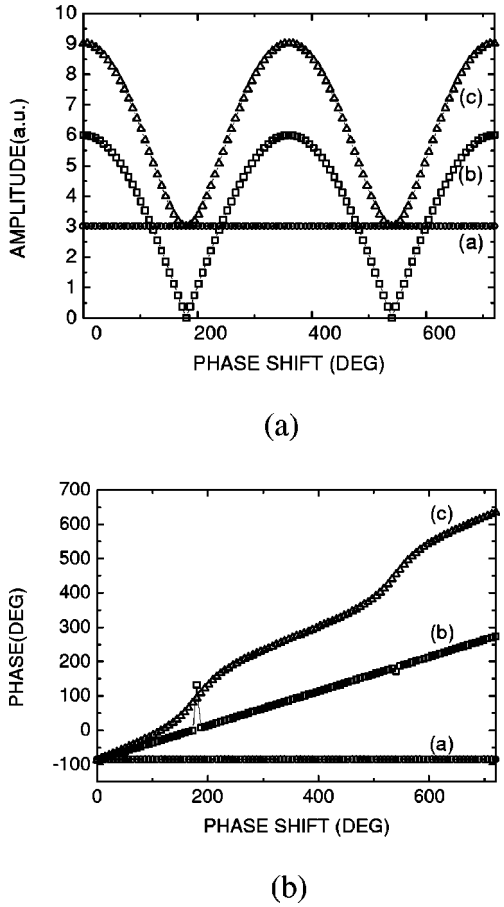


FIG. 4. Interferometric PPE signal vs phase shift between two incident beams at three different fluence ratios (a) $I_2/I_1=0$ ($I_2=0$), (b) $I_2/I_1=1.0$, (c) $I_2/I_1=2.0$. The off-line phase points in curve (b) at $\Delta\varphi=180°$ and 540° are due to the 0/0 operation (destructive interference).

### C. Two laser beams; no reference medium; single thermal-wave cavity

If the reference medium is absent (or if it is fixed at a very large distance compared to the thermal diffusion length

in the gas), one must set $m=0$, (or $e^{-\sigma_3 L_1}\rightarrow 0$) in Eq. (5). Assuming that the experimental setup is exposed to the same ambient gas (air) on both sides, the subscripts $1=2=3=4=g$, result in the following simplified expression:

$$V(\omega)=\frac{S(\omega)}{\sigma_p(1+b_{\mathrm{gp}})}\cdot\frac{(e^{\sigma_p d}-1+\gamma_{\mathrm{gp}}-\gamma_{\mathrm{gp}}e^{-\sigma_p d})[G_1(1+W_{21}e^{-2\sigma_g L})+2b_{\mathrm{gp}}G_3e^{-\sigma_g L}]+G_2'H_2'}{e^{\sigma_p d}(1+\gamma_{\mathrm{gp}}W_{21}e^{-2\sigma_g L})-\gamma_{\mathrm{gp}}e^{-\sigma_p d}(\gamma_{\mathrm{gp}}+W_{21}e^{-2\sigma_g L})}, \tag{9}$$

where $G_1$ is given by Eq. (6e), $G_2'\equiv(1-R_p)/k_p\sigma_p I_2 e^{j\Delta\varphi}$ and

$$H_2'\equiv(e^{\sigma_p d}-1)(1+\gamma_{\mathrm{gp}}W_{21}e^{-2\sigma_g L})+(1-e^{-\sigma_p d})(\gamma_{\mathrm{gp}}+W_{21}e^{-2\sigma_g L}). \tag{10}$$

It is easy to see that the difference between this case and the case discussed in Sec. III A is that the interference term $(G_2'H_2')$ appears in Eq. (9). This is an experimentally simple and useful case, because only the properties and the geometric parameters of the sample are involved. This situation is encountered in the study of optically transparent samples, in which a large base line signal from the direct optical transmission of the incident beam passing through the sample is usually the dominant factor limiting the sensitivity of the PPE measurement.[18] Fully destructive thermal-wave interferometry in the single-cavity mode can suppress the transmission base line and enhance the thermal component of the total PPE signal compared to case III B, where the interferometer in the absence of a sample can only detect optical (fluence) variations between the two incident laser beams.

A simple application of this PPE interferometric detection mode in the scanning imaging of a transparent optical material using the experimental setup illustrated in Fig. 5 is shown in Fig. 6. Two laser beams, which are split from one laser and modulated at the same frequency, are incident onto the front and rear surfaces of a PVDF detector. The relative intensities of the two beams can be adjusted by a linear intensity attenuator (neutral density filter), and the phase shift between the two beams is precisely controlled by adjusting an optical chopper. The reference is placed onto a single-axis micro stage for the purpose of scanning the cavity $(g_3)$ length between the reference and the PVDF element. The sample is mounted onto a three-axes micro stage, which allows for changing of the cavity $(g_2)$ length and the scanning imaging of the sample. A PVDF circular film, 52 $\mu$m thick and 1.2 cm in diameter, is mounted on an aluminum support with a hole in its base and acts as the PPE signal transducer.

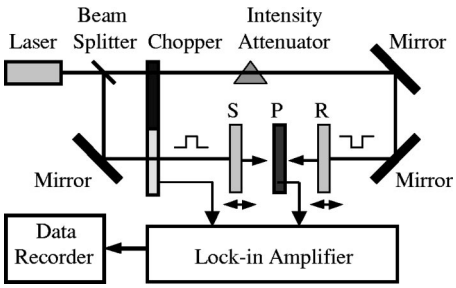


FIG. 5. Experimental setup for PPE thermal-wave interferometry. S: sample, P: PVDF detector; R: reference.

The thermal-wave signal from the PVDF is then fed into a lock-in amplifier (EG&G model 5210) without further amplification.

The PPE image shown in Fig. 6 is that of a Ti-sapphire laser disk with a diameter of 1.5 cm and thickness of 0.1295 cm. The experiment was conducted in the purely optical mode, with the Ti-sapphire disk having been placed far from the PVDF detector [i.e., $L\rightarrow\infty$ in Eq. (9)]. Thus, a very simple formula only involving the optical properties of the sample can be obtained

$$V(\omega)=\frac{S(\omega)(1-R_p)}{k_p\sigma_p^2(1+b_{\mathrm{gp}})}\cdot\frac{(e^{\sigma_p d}-1+\gamma_{\mathrm{gp}}-\gamma_{\mathrm{gp}}e^{-\sigma_p d})}{e^{\sigma_p d}-\gamma_{\mathrm{gp}}^2e^{-\sigma_p d}}\times\left[I_1\frac{(1-R_s)^2e^{-\beta_s l}}{1-R_s^2e^{-2\beta_s l}}+I_2e^{j\Delta\varphi}\right]. \tag{11}$$

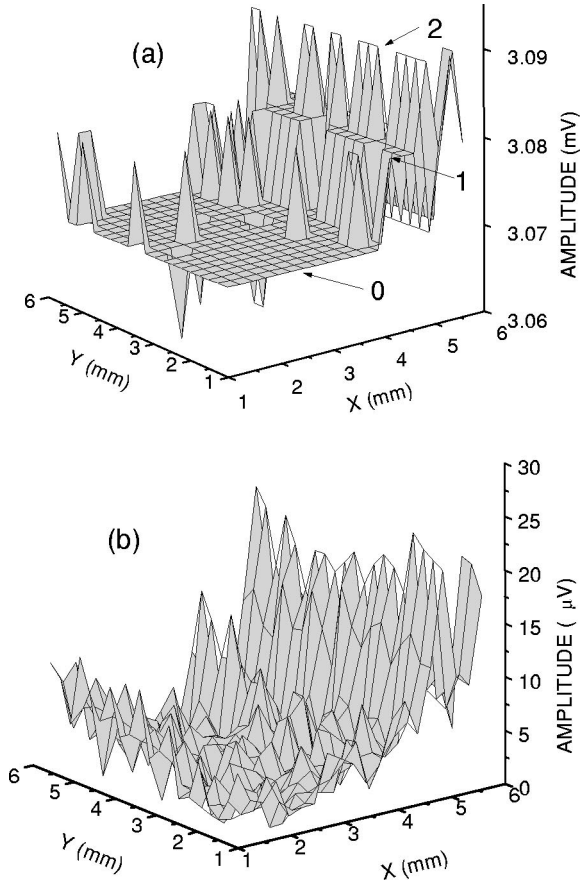


FIG. 6. Comparison of PPE scanned images of a Ti-sapphire laser rod using (a) the single-beam method, case A, (b) the optical-beam PPE thermal-wave interferometer, case C.

Once the PVDF detector and the measuring system are chosen, the first two ratios in Eq. (11) become fixed constants. If the phase shift $\Delta\varphi = 180°$ and the relative fluences of the two beams $(I_1, I_2)$ are adjusted such that the output signal is zero at the onset of the scanning, this effectively zeros the term in brackets in Eq. (11). In principle, the ratio $I_1/I_2$ resulting from this zeroing operation yields an accurate value of the optical absorption coefficient $\beta_s$ of the transparent material, if its surface reflectance $R_s$ is known or remains constant throughout the scan. After the single-point zeroing correction, any optical defects and/or surface or bulk nonuniformities will introduce changes in $R_s$ and/or $\beta_s$ in Eq. (11), which can be sensitively monitored as a signal departure from the noise-limited base line. Moreover, another advantage of this scanning imaging technique is that the noise component due to intensity fluctuations or drift of the common laser-beam source is also coherently suppressed. Figure 6 shows two PPE images of a $6\times 6\ \mathrm{mm}^2$ area at the center of the laser disk. Both the single-beam method and the thermal-wave interferometric method yield the same basic image of this area. In the region labeled $x = 4-6$ mm, both images show higher transmission but less uniformity than the region labeled $x = 1-4$ mm. The highest optical uniformity of this material is located in the region bounded between $x = 1-4$ mm and $y = 1-4$ mm, as deduced from the interferometric image, Fig. 6(b). The single-beam image, Fig. 6(a), shows almost perfect flatness in this region caused by lack of dynamic range, a result of the dominating optical transmission signal base line. The thermal-wave interferometric image, however, shows the surface morphology amplified by a factor of approx. 300. The most significant difference between the two images occurs in the region bounded by $x = 1-3$ mm and $y = 4-6$ mm. The thermal-wave-interference image shows a gradual and continuous increase in the amplitude from $\sim 0-12\ \mu$V with the practical resolution of $\sim 1\ \mu$V, while the single-beam image only exhibits three levels (labeled 0, 1, and 2) limited by lack of signal quantization. In conclusion, Fig. 6 shows that optical imaging with PPE interferometric thermal waves is superior to single-beam imaging with respect to sensitivity, resolution and signal dynamic range. Therefore, this technique is a promising new tool for optical scanning imaging.

### D. Two laser beams; two thermal-wave cavities

In view of the structure of Eq. (5), it can be seen that the first term in the numerator is due to the front incident beam, with the $G_1$ term representing the contribution from the direct transmission of the incident light and the $G_3$ term being the thermal contribution due to the optical-to-thermal conversion process in the sample. The same situation occurs with the rear beam and the reference sample: here $G_2$ and $G_4$ represent the direct transmission of the rear beam and the optical-to-thermal conversion process at the reference sample, respectively. If both cavity walls are opaque, $G_1$ and $G_2$ are equal to zero, with only the contributions from $G_3$ and $G_4$ appearing in Eq. (5). By contrast, if both cavity walls are highly transparent, only contributions from $G_1$ and $G_2$ have to be taken into account due to the comparatively negligible contributions from the $G_3$ and $G_4$ terms. Therefore, two different operational mechanisms and configurations with either transparent or opaque walls can be employed and will be discussed separately.

#### *1. Highly transparent cavity walls; spectroscopic mode*

Due to the very weak absorption coefficient of the sample and the reference, the thermal contributions to the overall PPE signal resulting from the optical-to-thermal conversion processes after the optical absorption are very small. Theoretical simulations of Eq. (5) show that the contributions from the direct transmissions of the front and rear beam onto the PVDF detector ($G_1$ and $G_2$ terms) are 3–4 orders of magnitude greater than contributions from the optical absorption processes ($G_3$ and $G_4$ terms) for all cavity lengths. Therefore, the overall PPE signal can be simplified by neglecting $G_3$ and $G_4$ terms in Eq. (5). Owing to this fact, a major application corresponding to this case can be expected in the measurements of the optical properties of the sample which are included in the $G_1$ term if the reference is well defined. For this application, the entire measurement system is assumed to be exposed to the same gaseous ambient in practice. By setting subscripts $1=2=3=4=g$ in Eq. (5), the overall PPE signal reduces to

$$V(\omega) = \frac{S(\omega)}{\sigma_p(1+b_{\mathrm{gp}})}\,\frac{H_1G_1(1+W_{21}e^{-2\sigma_g L})+H_2G_2(1+V_{34}e^{-2\sigma_g L_1})}{e^{\sigma_p d}(1+\gamma_{\mathrm{gp}}V_{34}e^{-2\sigma_g L_1})(1+\gamma_{\mathrm{gp}}W_{21}e^{-2\sigma_g L})-e^{-\sigma_p d}(\gamma_{\mathrm{gp}}+W_{21}e^{-2\sigma_g L})(\gamma_{\mathrm{gp}}+V_{34}e^{-2\sigma_g L_1})}. \tag{12}$$

The symbols used in Eq. (12) have the same meanings as those in Eq. (5). As expected, if both sample and reference are placed far away from the PVDF detector, Eq. (12) reduces to case III B above, with $I_1$ and $I_2$ being replaced by $G_1$ and $G_2$, respectively. There is no advantage of the present geometry over that of case III B in the purely optical mode. In fact, the simplicity of that configuration, without the complicating presence of the reference sample, must be noted. The advantage of the double thermal-wave cavity appears in the near field, where both sample and reference are placed in thermal contact with the PVDF detector, i.e., the cavity lengths have to be smaller than one thermal diffusion length in the gas. Figure 7 shows the PPE signal resulting from scanning the sample cavity length $L$ from the purely optical mode to the thermally contacting mode, while the reference cavity length is fixed at a thermally contacting $L_1 = 0.02$ cm. To simulate the effect of the optical absorption coefficient $(\beta_s)$ of the sample on the PPE output signal, the

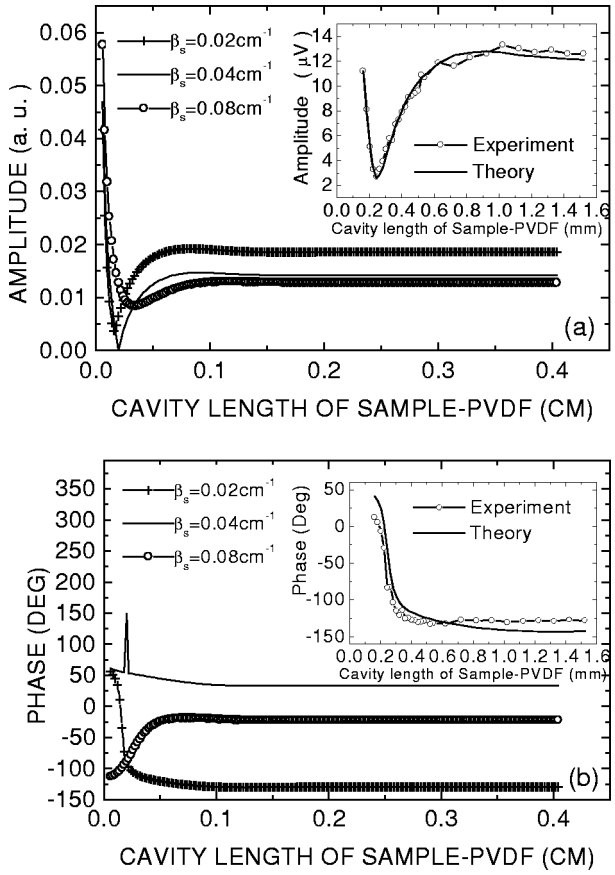


FIG. 7. Theoretical behavior of a differential PPE interferometric sensor at various cavity lengths $L$ and $f=10$ Hz. (a) Amplitude, (b) phase. Insets: experimental results from Schott BK7 glass sample and reference, and theoretical fits.

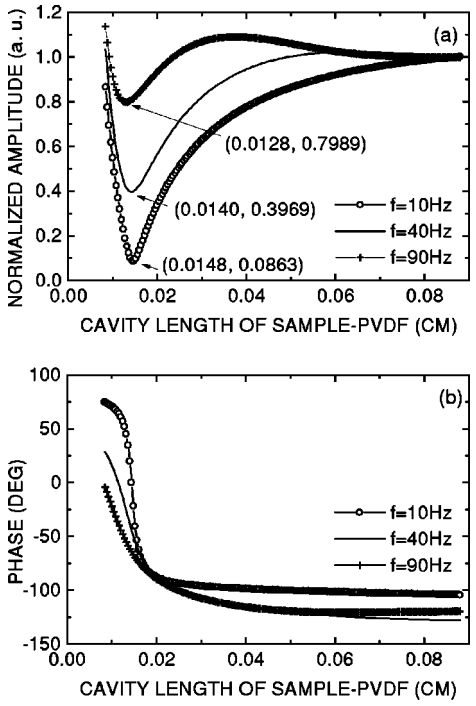


FIG. 8. Theoretical behavior of a destructive interferometric PPE sensor at three modulation frequencies $f=10$, 40, and 90 Hz. (a) Amplitude, (b) phase. The number pairs shown in (a) indicate the coordinate positions of the minimum points for each curve.

sample and the reference were assumed to have the same thickness and thermal properties but different optical absorption coefficients. Here parameters of Schott BK7 window glass[19] are used: $l=m=0.3$ cm, $R_s=R_r=0.07$, $k_s=k_r=1.114\times10^{-2}$ W/cm k, $\alpha_s=\alpha_r=5.173\times10^{-3}$ cm$^2$/s, and $\beta_r=0.04\,\mathrm{cm}^{-1}$. The modulation frequency is fixed at $f=26.6$ Hz and the entire system operates in open air. Figure 7 shows that the theoretical outputs in both amplitude and phase channels are very sensitive to the change in the optical absorption coefficient of the sample ($\beta_s$). As expected from symmetry, the output in amplitude has a sharp dip to zero when scanning the sample-PVDF cavity length to the distance $L=L_1$ in the case of $\beta_s=\beta_r$. Under those same conditions, the phase being the ratio of the quadrature and the in-phase signal (both zero) becomes undetermined [a spike in Fig. 7(b)]; compare curve (b) in Fig. 4(b). If $\beta_s$ is slightly different from $\beta_r$, the amplitude minimum is not equal to zero, and its position depends sensitively on the difference between the values of these two parameters [Fig. 7(a)]. In the insets of Fig. 7, experimental results are shown to demonstrate the capability of the method. In the experiment, two ''identical'' commercial Schott BK7 window glasses, 0.3 cm thick were used. The experimental conditions were the same as those assumed in the theoretical simulation. The relative intensities and the phase shift between the two incident beams were adjusted, such that the output equals zero in the absence of both the sample and the reference: $I_1=I_2$ and $\Delta\varphi=180°$. Then the reference and sample were put in place, in thermal contact with the PVDF, and the sample cavity length $L$ was scanned. Fitting experimental data to amplitude is preferable, due to the sharp minimum in this PPE channel. By fitting the amplitude of the PPE signal to Eq. (12), a difference in optical absorption coefficient of $\Delta\beta=(\beta_r-\beta_s)=9.7\times10^{-3}\,\mathrm{cm}^{-1}$ between the sample and the reference was found. Then, the PPE phase was fitted using the $\Delta\beta$ value obtained from the amplitude fit to ascertain consistency and validity. Numerical fitting further showed that this relative measurement is independent of the value of the optical absorption coefficient of the reference ($\beta_r$), which must be used in the fitting, in a wide range of optical absorption coefficients from $10^{-3}$ to $10^{-1}\,\mathrm{cm}^{-1}$, which is the case for most optical glasses. Therefore, thermal-wave destructive interferometry provides a very useful method for measuring very small differences in the optical absorption coefficient of two samples quantitatively. The absolute value of the optical absorption coefficient of the sample can also be measured, if $\beta_r$ is known.

To optimize the measurement, different modulation frequencies can be considered. Figure 8 shows the effect of the modulation frequency on the PPE output signal, in which the cavity length at the reference side is fixed at 0.02 cm, and the absorption coefficients of the sample and the reference are assumed to be $\beta_r=0.04$ and $\beta_s=0.03\,\mathrm{cm}^{-1}$, respectively. Figure 8(a) shows that higher modulation frequency gives a greater positional shift from the reference position and a greater deviation of the minimum output from zero. Therefore, higher modulation frequency provides higher sensitivity

of the measurement in the amplitude channel. However, higher frequency will produce a smaller output signal, hence lower measurement signal-to-noise ratio, and will also produce smaller phase variation [Fig. 8(b)]. As a result, an optimal trade-off operation frequency should be chosen for a given experiment.

### 2. Opaque cavity walls; thermophysical mode

In the case of entirely opaque walls, no direct optical transmission of the incident light is possible. The PPE signal is due to interfering thermal waves originating in optical-to-thermal power conversion of the saturated[7] optical absorption of the incident light on the exterior surfaces of the sample and the reference. These thermal waves are (mainly) conductively transmitted to the PVDF. The demodulated signal should be zero if the gases in the two cavities are the same, the opaque sample and reference are identical geometrically, and thermally, and the two beams are adjusted such that $I_1=I_2$, with $\Delta\varphi=180°$ (fully destructive interference). If the gaseous ambient in one of the cavities is changed, the symmetry between the two thermal wave cavities is broken, and thus a net output signal is expected to appear. Therefore, a highly sensitive differential thermophysical gas sensor can be designed based on this principle. For the purposes of designing this sensor, the foregoing theory of the PPE interferometer suggests that totally opaque materials must be used for both sample and reference cavity walls to reduce the complexity of the theoretical analysis and experimental operation. It can be further assumed that the PVDF is thermally thick, the gas ambient in regions $g1$, $g2$, and $g4$ is the same in the simplest case, while the gas under investigation is confined in region $g3$ (Fig. 1). Under these conditions, the following values are inserted in Eq. (5): subscripts $1=4=2$ $(\neq 3)$ and $r=s$; totally opaque sample and reference cavity ''walls'' give $e^{-\beta_s l}\to 0$, $e^{-\beta_{rm}}\to 0$, which leads to $G_1=0$ and $G_2=0$. Equation (5) reduces to

$$V(\omega)=\frac{2S(\omega)e^{-\sigma_s l}}{k_p\sigma_p^2(1+b_{2s})}\cdot\frac{1}{1-\gamma_{2p}\gamma_{2s}e^{-2\sigma_2 L}}\cdot\frac{1}{1-\gamma_{3p}\gamma_{3s}e^{-2\sigma_3 L_1}}\times\left[\frac{I_1 b_{2s}(1-\gamma_{3p}\gamma_{3s}e^{-2\sigma_3 L_1})e^{-\sigma_2 L}}{(1+b_{2p})(1+b_{2s})(1-\gamma_{2s}^2 e^{-2\sigma_s l})}+\frac{I_2 e^{j\Delta\varphi}b_{3s}(1-\gamma_{2p}\gamma_{2s}e^{-2\sigma_2 L})e^{-\sigma_3 L_1}}{(1+b_{3p})(1+b_{3s})(1-\gamma_{2s}\gamma_{3s}e^{-2\sigma_s l})}\right]. \quad (13)$$

The output signal is a complex function of the thermal coupling coefficients between the intracavity gases and the cavity walls. However, once the cavity walls and the geometric parameters of the system are fixed, the signal is only a function of the intracavity gases, the thermophysical properties of which are included very sensitively in the exponential functions in Eq. (13), and less so in the thermal coupling coefficients $b_{ij}$ and $\gamma_{ij}$. Figure 9 shows the characteristics of the output signal versus the cavity length $L$ on the sample side for several thermal diffusivities of the test gas in that intracavity space. The cavity length at the reference side is fixed at $L_1=0.03$ cm. In the simulation, the parameters of aluminum foil walls were used: $\alpha_s=0.98$ cm$^2$/s, $k_s=2.37$ W/cm K,[20] $l=15$ $\mu$m; regions $g1$, $g2$ and $g4$ are exposed to air (i.e., $\alpha_2=0.22$ cm$^2$/s, $k_2=2.62\times10^{-4}$ W/cm K), and $I_1=I_2$, $\Delta\varphi=180°$. The modulation frequency is 30 Hz. As can be seen, if the gases in the two cavities are different, the amplitude minimum line shape and its position vary sensitively with the relative thermal diffusivities of the two gases: lower diffusivity of the test gas results in a sharper and deeper amplitude minimum line shape positioned closer to the detector. The opposite is true for higher test-gas diffusivity. As expected, the output signal decreases to zero when the scanned cavity length on the sample side is equal to $L_1$ when the gases in the two cavities are identical, and the phase also becomes indeterminate at the point of $L=L_1$ [see also Figs 4(b), curve (b), and 7(b)]. The signal phase past the indeterminate point, however, is a very sensitive function of the test-gas thermal diffusivity [Fig. 9(b)], and switches from lead to lag as the test gas turns from a poorer to a better conductor than the reference. The dual-cavity gas sensor is expected to be more sensitive to test-gas thermophysical properties (diffusivity and conductivity) than its single-cavity counterpart,[5] owing to the suppression of the thermal base line and the real-time differential measurement effected by this novel cavity design.

A quantitative way to monitor minute changes in thermophysical properties of the intracavity gases can be devised. In this measurement method, the two cavity lengths are fixed at the same value, i.e., $L=L_1$, and the output signal is calibrated to zero when the two cavities are exposed to the same gaseous medium. Thereafter, any relative changes between the two intracavity gases will be sensitively monitored by a nonzero output. Figures 10 and 11 show how this differential gas sensor is expected to behave theoretically at several cavity lengths $L$, such that $L=L_1$ and various modulation frequencies $(f)$ using Eq. (13). The same parameters as those in Fig. 9 were used in the simulation. In Fig. 10, the values of thermal diffusivity $(\alpha_3)$ and conductivity $(k_3)$ of the intracavity gas were assumed to depart linearly from those of the ambient (background air) with the forms $\alpha_3=[0.22+n*1.6\times10^{-3}]$ cm$^2$/s and $k_3=[2.62+n*8\times10^{-3}]\times10^{-4}$ W/cm K, where $n$ is an integer from 0 to 125. At the starting point $(n=0)$ of Fig. 10, the parameters of the test gas in region 3 are the same as those in region 2 (air). Therefore, the output signal amplitude at this point is zero and the phase is indeterminate due to fully destructive thermal-wave interference inside the PVDF. Figure 10 shows that the sensitivity of the sensor in the amplitude channel to the change in thermophysical properties of the gas is enhanced with decreasing cavity length, while the phase channel shows the opposite trend feature from the amplitude. A similar effect can be seen in Fig. 11, which shows that the sensitivity of the sensor in the amplitude channel is enhanced with decreasing modulation frequency, as expected, since the intracavity thermal-wave power reaching the surface of the sensor is increased. In practice, however, lower frequency operation of the interferometer will result in a larger overall system $(1/f)$ noise.

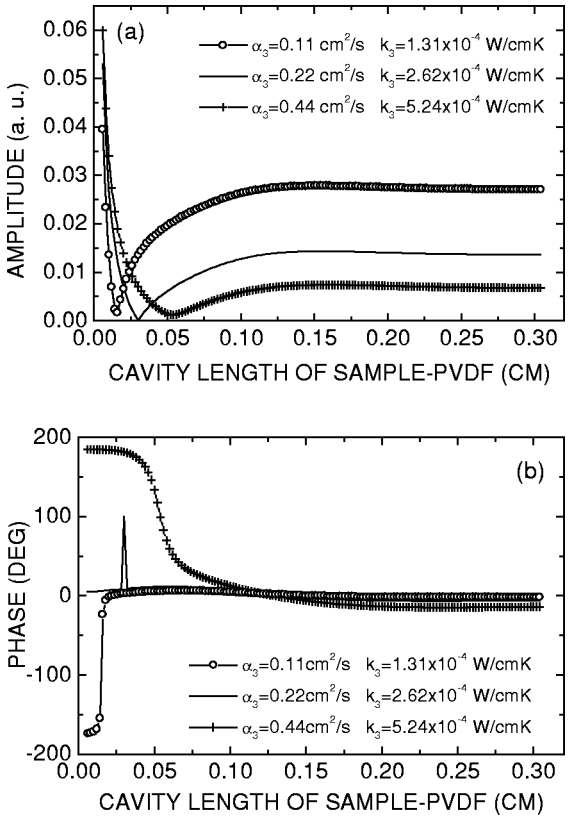


FIG. 9. Theoretical behavior of the destructive interferometric thermophysical PPE gas sensor operating in air (reference) and in a gaseous ambient, with three different thermal diffusivities. (a) Amplitude, (b) phase.

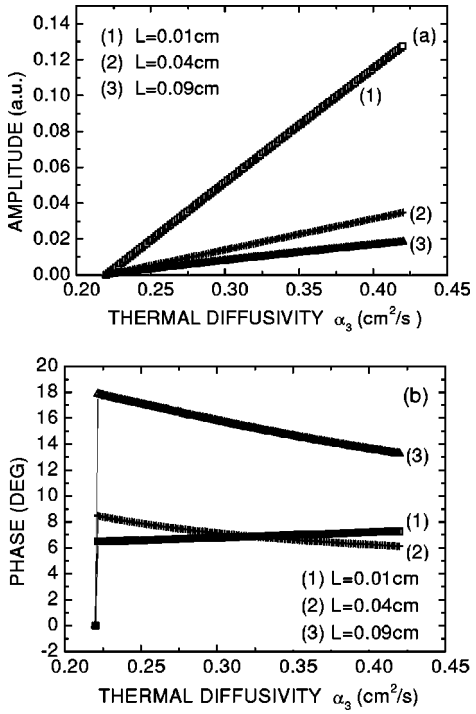


FIG. 10. (a) Theoretical amplitude, and (b) phase of the destructive interferometric thermophysical PPE gas sensor signal as a function of the intracavity-gas thermal diffusivity, with cavity length as a parameter.

## IV. DISCUSSION

The successful development of photopyroelectric thermal-wave interferometry must be placed in the proper physical context, in order to understand the peculiar nature of ''thermal-wave interferometry.'' A discussion of the nature of thermal standing-wave patterns leading to the single-cavity sensor consistent with the heat-conduction continuity equation (otherwise known as Fourier's law)

$$-k\nabla T(\mathbf{r},\mathbf{t})=\mathbf{F}(\mathbf{r},\mathbf{t}) \tag{14}$$

has been given elsewhere.[5] Here $\mathbf{F}$ is the thermal-wave flux and $k$ is the thermal conductivity of the medium in which thermal waves propagate diffusively. The essence of the wavelike nature of thermal waves lies in the fact that diffusive temperature-wave propagation cannot sustain reflections at the boundary walls of the cavity (or cavities), where the thermophysical properties change abruptly. This is so because conduction heat transfer is unidirectional and only activated by existing temperature gradients, which generate net heat fluxes in the appropriate direction of decreasing temperature in the cavity according to the continuity equation, Eq. (14). This is unlike propagating wave fields (acoustic, optical), where a definite mode structure exists, which stems from a well-defined completeness relation linking temporally orthogonal eigenfunctions of the motion.[21] In the thermal-wave field there are no orthogonal temporal eigenmodes, and thus there is no completeness relation to assure the energy conservation of a mode structure with well-defined energy content (harmonic Fourier spectrum), a prerequisite for conventional wave phenomena (e.g., reflection, refraction, diffraction and polarization). Nevertheless, the intracavity space energy distribution can be sufficiently described by the math-

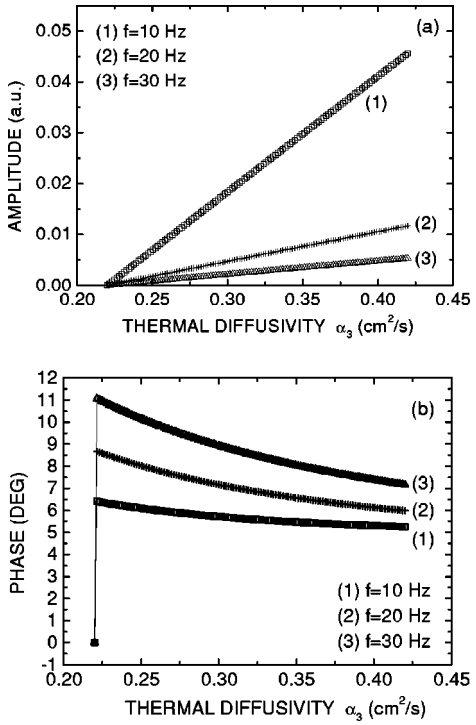


FIG. 11. (a) Theoretical amplitude, and (b) phase of the destructive interferometric thermophysical PPE gas sensor signal as a function of the intracavity-gas thermal diffusivity, with modulation frequency as a parameter.

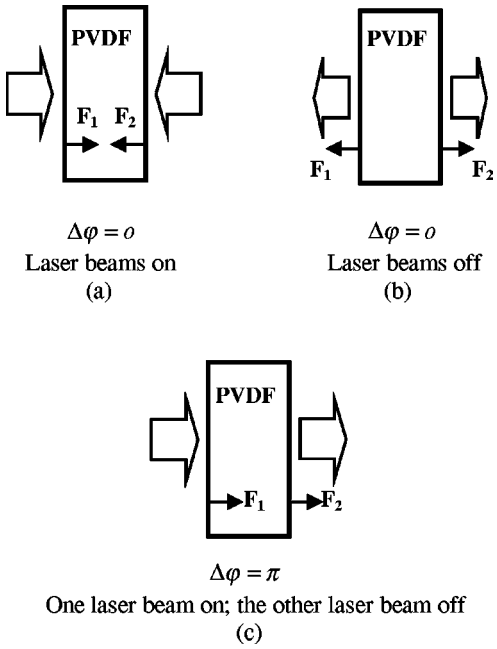


FIG. 12. Physical origins of two-beam thermal-wave interferometry: (a) in-phase operation, maximum of fully constructive interference, (b) in-phase operation, minimum of fully constructive interference, and (c) out-of-phase operation, fully destructive interference.

ematical equivalent of a thermal standing-wave pattern formed by the rate of coherent thermal oscillations transporting an amount of net power across the cavity length. The thermal transport rate is thus controlled by local phase relations of the oscillating thermal energy, fixed by the source and the presence of the cavity wall(s).[5] This intracavity power confinement can be mathematically described by a standing thermal-wave pattern as a function of the intracavity coordinate. Based on this understanding of the wave nature of temporal thermal oscillations as coherent phase superpositions of unidirectionally transported power, Fig. 12 helps describe the physical nature of (photo)thermal-wave dual-beam interferometry introduced in this work: only with the introduction of opposing temperature-wave gradients (thermal fluxes) in the form of two optothermal heat sources, can propagation of thermal power be achieved in the direction opposite to an existing gradient (flux $F_j$; $j=1,2$), as shown in Fig. 12. In this situation, interferometric phenomena can be described as linear superpositions of the two unidirectional thermal-wave fields launched photothermally from opposite directions. It is to be noted that the role of the optical beams is limited in the energy conversion process of the modulated beams into thermal-wave surface sources and that no optical interferences occur anywhere in the configurations of Figs. 1 or 12 (whence the name ''purely thermal-wave interferometry''). Assuming equal laser fluences on both sides of the PPE transducer, when both beams are on (in-phase operation), the *net* thermal flux into the PVDF detector is maximum, as the *inward* fluxes from both surfaces add across the thickness of the transducer to generate the maximum possible temperature at that instant [Figs. 4(a) and 4(b) and 12(a)]. Conversely, when both beams are off (still in-phase operation), the stored thermal energy conductively diffuses out of the PVDF from both surfaces. This creates the maximum *outward* flux resulting in the minimum possible temperature across the transducer at that instant of the oscillation cycle [Figs. 4(a) and 4(b) and 12(b)]. The linear superposition of the two thermal-wave fields (front and back surface) yields the mathematical equivalent of *constructive interference* of the thermal waves generated in the bulk of the film, in the language of conventional propagating wave fields.[22,23] On the other hand, when the two laser beams are out of phase by exactly 180°, the *inward* thermal flux from the surface temperature gradient due to the incidence of one beam is exactly balanced by the *outward* flux from the opposite-surface temperature gradient due to the absence of the other beam at all instants of the oscillation cycle [Fig. 12(c)]. The result is that the overall thermal content of the transducer remains dynamically fixed at all times, yielding a (theoretically) zero lock-in output. Again, the linear superposition of the two fluxes across the film results in the mathematical equivalent of fully destructive interference of the two out-of-phase thermal waves, in the language of propagating fields. The operation of the present PPE interferometric device is based on the base line suppression afforded by the dynamic steady state flux balance of configuration Fig. 12(c).

## V. CONCLUSIONS

A novel thermal-wave interferometric device was demonstrated using photopyroelectric detection. A one-dimensional theoretical approach to the PPE signal output of the interferometer was developed and several operation modes were examined. The figure-of-merit (one-beam/two-beam signal amplitude ratio) of the new instrument was estimated to be on the order of 3000 if a 5 mW laser was employed. Both theoretically and experimentally, it was found that optical-mode operation of the new PPE interferometer yields high-resolution imaging of optical structures, which are usually limited by the base line of single-ended PPE operation. A PPE measurement of the differential optical absorption coefficient between nominally identically manufactured transparent solids (Schott BK7 window glasses) was performed in the thermally contacting mode. In addition, high-resolution scanned images of optical defects in a Ti-sapphire laser disk were obtained. The new device is expected to be useful for optical studies and scanning imaging of highly transparent media, as well as a high-resolution thermophysical gas sensor.

## ACKNOWLEDGMENT

The support of a Research Grant from the Natural Sciences and Engineering Research Council of Canada (NSERC) is gratefully acknowledged.

## APPENDIX

Complex quantities used in the general pyroelectric signal [Eq. (5)]

$$H_1=(e^{\sigma_p d}-1)(1+\gamma_{3p}V_{34}e^{-2\sigma_3 L_1}) + (1-e^{-\sigma_p d})(\gamma_{3p}+V_{34}e^{-2\sigma_3 L_1}), \quad \text{(A1)}$$

$$H_2=(e^{\sigma_p d}-1)(1+\gamma_{2p}W_{21}e^{-2\sigma_2 L}) + (1-e^{-\sigma_p d})(\gamma_{2p}+W_{21}e^{-2\sigma_2 L}), \tag{A2}$$

$$G_3=\frac{2Q_1-Q_2(1+b_{1s})e^{\sigma_s l}+Q_3(1-b_{1s})e^{-\sigma_s l}}{(1+b_{1s})(1+b_{2s})(e^{\sigma_s l}-\gamma_{1s}\gamma_{2s}e^{-\sigma_s l})} \tag{A3}$$

with

$$Q_1=E_s[b_{1s}(N_1+N_2e^{-2\beta_s l})+r_s(N_1-N_2e^{-2\beta_s l})], \tag{A4}$$

$$Q_2=E_s e^{-\beta_s l}[N_1+N_2+r_s(N_1-N_2)], \tag{A5}$$

$$Q_3=E_s e^{-\beta_s l}[N_1+N_2-r_s(N_1-N_2)], \tag{A6}$$

$$E_s=\frac{I_1\eta_s\beta_s}{2k_s(\beta_s^2-\sigma_s^2)}\cdot\frac{1-R_s}{1-R_s^2e^{-2\beta_s l}}, \tag{A7}$$

$$r_s=\beta_s/\sigma_s \tag{A8}$$

and

$$G_4=\frac{2P_1+P_2(1+b_{4r})e^{\sigma_r m}-P_3(1-b_{4r})e^{-\sigma_r m}}{(1+b_{3r})(1+b_{4r})(e^{\sigma_r m}-\gamma_{3r}\gamma_{4r}e^{\sigma_r m})} \tag{A9}$$

with

$$P_1=E_r[b_{4r}(N_{1r}+N_{2r}e^{-2\beta_r m})+r_r(N_{1r}-N_{2r}e^{-2\beta_r m})], \tag{A10}$$

$$P_2=-E_r e^{-\beta_r m}[N_{1r}+N_{2r}+r_r(N_{1r}-N_{2r})], \tag{A11}$$

$$P_3=-E_r e^{-\beta_r m}[N_{1r}+N_{2r}-r_r(N_{1r}-N_{2r})], \tag{A12}$$

$$E_r=\frac{I_2e^{j\Delta\varphi}\eta_r\beta_r}{2k_r(\beta_r^2-\sigma_r^2)}\cdot\frac{1-R_r}{1-R_r^2e^{-2\beta_r m}}, \tag{A13}$$

$$r_r=\beta_r/\sigma_r. \tag{A14}$$


[1] A. Mandelis, Chem. Phys. Lett. **108**, 388 (1984); H. Coufal, Appl. Phys. Lett. **44**, 59 (1984).
[2] H. Coufal and A. Mandelis, Ferroelectrics **118**, 379 (1991).
[3] A. Mandelis, J. Vanniasinkam, and S. Budhudu, Phys. Rev. B **48**, 6808 (1993).
[4] M. Chirtoc and G. Mihailescu, Phys. Rev. B **40**, 9606 (1989).
[5] J. Shen and A. Mandelis, Rev. Sci. Instrum. **66**, 4999 (1995).
[6] A. Mandelis and K. F. Leung, J. Opt. Soc. Am. A **8**, 186 (1991).
[7] A. Mandelis and M. M. Zver, J. Appl. Phys. **57**, 4421 (1985).
[8] J. Shen, A. Mandelis, and B. D. Aloysius, Int. J. Thermophys. **17**, 1241 (1996).
[9] J. Shen, A. Mandelis, and H. Tsai, Rev. Sci. Instrum. **69**, 197 (1998).
[10] M. Bertolotti, G. L. Liakhou, R. Li Voti, S. Paoloni, and C. Sibilia, Int. J. Thermophys. **19**, 603 (1998).
[11] M. Chirtoc, D. Bicanic, and V. Tosa, Rev. Sci. Instrum. **62**, 2257 (1991).
[12] H. Coufal, F. Trager, T. J. Chuang, and A. C. Tam, Surf. Sci. **145**, L504 (1984).
[13] Z. Sodnik and H. J. Tiziani, Opt. Commun. **58**, 295 (1986).
[14] L. Wawrzyniuk and G. Dymny, Opt. Eng. (Bellingham) **36**, 1602 (1997).
[15] H. G. Walther, K. Friedrich, K. Haupt, K. Muratikov, and A. Glazov, Appl. Phys. Lett. **57**, 1600 (1990).
[16] *Kynar$^{TM}$ Piezo Film Technical Manual* (Pennwalt, King of Prussia, PA, 1983), p. 17.
[17] C.-H. Wang and A. Mandelis, Rev. Sci. Instrum. (submitted).
[18] J. Vanniasinkam, A. Mandelis, S. Buddhudu, and M. Kokta, J. Appl. Phys. **75**, 8090 (1994).
[19] *Schott Optical Glass Catalog* (Schott Glass, Duryea, PA, 1996).
[20] *CRC Handbook of Chemistry and Physics*, 74th ed., edited by D. R. Lide (Chemical Rubber, Cleveland, OH, 1993), pp. 12–134 (Al).
[21] P. M. Morse and H. Feshbach, *Methods of Theoretical Physics* (McGraw–Hill, New York, 1953), Vol. I, Chap. 7.
[22] M. Born and E. Wolf, *Principles of Optics* (Pergamon, New York, 1980).
[23] R. E. Berg and D. G. Stork, *The Physics of Sound* (Prentice–Hall, Englewood Cliffs, NJ, 1995), Chap. 2, p. 39.